ACS Photonics

Letter

pubs.acs.org/journal/apchd5

Highly Sensitive, Gate-Tunable, Room-Temperature Mid-Infrared Photodetection Based on Graphene–Bi_2Se_3 Heterostructure

Jaeseok Kim,[†,◆,▽] Sungjoon Park,[†,▽] Houk Jang,[†] Nikesh Koirala,[‡] Jae-Bok Lee,[†] Un Jeong Kim,[§] Hong-Seok Lee,[§] Young-Geun Roh,[§] Hyangsook Lee,[⊥] Sangwan Sim,[†] Soonyoung Cha,[†] Chihun In,[†] Jun Park,[†] Jekwan Lee,[†] Minji Noh,[†] Jisoo Moon,[‡] Maryam Salehi,[∥] Jiho Sung,[¶] Sang-Soo Chee,[#] Moon-Ho Ham,[#] Moon-Ho Jo,[¶,⬡] Seongshik Oh,[‡,□] Jong-Hyun Ahn,[†] Sung Woo Hwang,[§] Dohun Kim,[*,Ω] and Hyunyong Choi[*,†]

[†]School of Electrical and Electronic Engineering, Yonsei University, Seoul 120-749, Korea

[◆]Next Generation Media Team, DMC R&D Center, Samsung Electronics Co., Seoul R&D Campus, 34, Seongchon-Gil, Seocho-Gu, Seoul 06765, Korea

[‡]Department of Physics and Astronomy, Rutgers, [∥]Department of Materials Science and Engineering, Rutgers, and [□]Institute for Advanced Materials, Devices and Nanotechnology, Rutgers, The State University of New Jersey, Piscataway, New Jersey 08854, United States

[§]Device Lab and [⊥]AE Group, Samsung Advanced Institute of Technology, Samsung Electronics Co., Suwon 443-803, Korea

[¶]Division of Advanced Materials Science and [⬡]Department of Materials Science and Engineering, Pohang University of Science and Technology (POSTECH), 77 Cheongam-Ro, Pohang 790-784, Korea

[#]School of Materials Science and Engineering, Gwangju Institute of Science & Technology, 123 Cheomdangwagi-ro Buk-gu, Gwangju 61005, Korea

[Ω]Department of Physics and Astronomy, Seoul National University, Seoul 08826, Korea

Supporting Information

ABSTRACT: Broadband detection of mid-infrared (IR) photons extends to advanced optoelectronic applications such as imaging, sensing, and telecommunications. While graphene offers an attractive platform for broadband visible/IR photodetection, previous efforts to improve its responsivity, for example, by integrating light-absorbing colloids or waveguide or antenna fabrication, were achieved at the cost of reduced photon detection bandwidth. In this work, we demonstrate room-temperature operation of a novel mid-IR photodetector based on a graphene–Bi_2Se_3 heterostructure showing broadband detection and high responsivity (1.97 and 8.18 A/W at mid- and near-IR, respectively), in which simultaneous improvement of the spectral range and responsivity is achieved via exploiting broadband absorption of mid-IR and IR photons in a small-band-gap Bi_2Se_3 topological insulator and efficient hot carrier separation and strong photogating across the Bi_2Se_3/graphene interface. With sufficient room for further improvement by interface engineering, our results show a promising route to realize ultrabroadband, high-responsivity hot-carrier optoelectronics at room temperature.

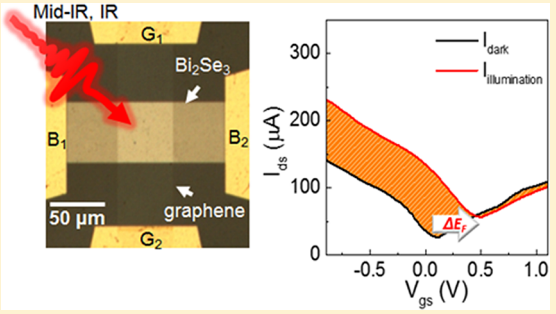

KEYWORDS: *photodetectors, mid-infrared photodetection, topological insulators, graphene, heterostructure, photogating effect*

Although graphene has a unique advantage for hot-electron photodetection in that photons at all frequencies can generate electron–hole (e–h) pairs in gapless graphene,[1−5] intrinsically low optical absorption (~2.3%) and fast relaxation (picosecond time scale) of photoexcited hot carriers[6,7] set limits to using intrinsic graphene as a sensitive photodetector. Techniques such as graphene plasmons[8] or microcavities[9,10] and graphene–metal junctions[11] to improve responsivity rely on enhanced light–matter interaction by resonant light absorption,[12] and photothermoelectric type detectors[13−15] utilize low heat capacity of electrons in two-dimensional graphene, thereby producing a large thermal gradient. However, resonant light absorption results in a reduced spectral range for photodetection, while photodetectors based on a photothermoelectric effect often suffer from a small working area, and so far the responsivity is limited to tens of mA W^{-1}.

With recent development in fabricating low-dimensional heterostructures, hybrid structures of graphene with other materials have emerged as alternative pathways to realize highly sensitive and broadband IR photodetection. The key idea in

Received: December 7, 2016
Published: February 15, 2017

DOI: 10.1021/acsphotonics.6b00972
ACS Photonics 2017, 4, 482−488

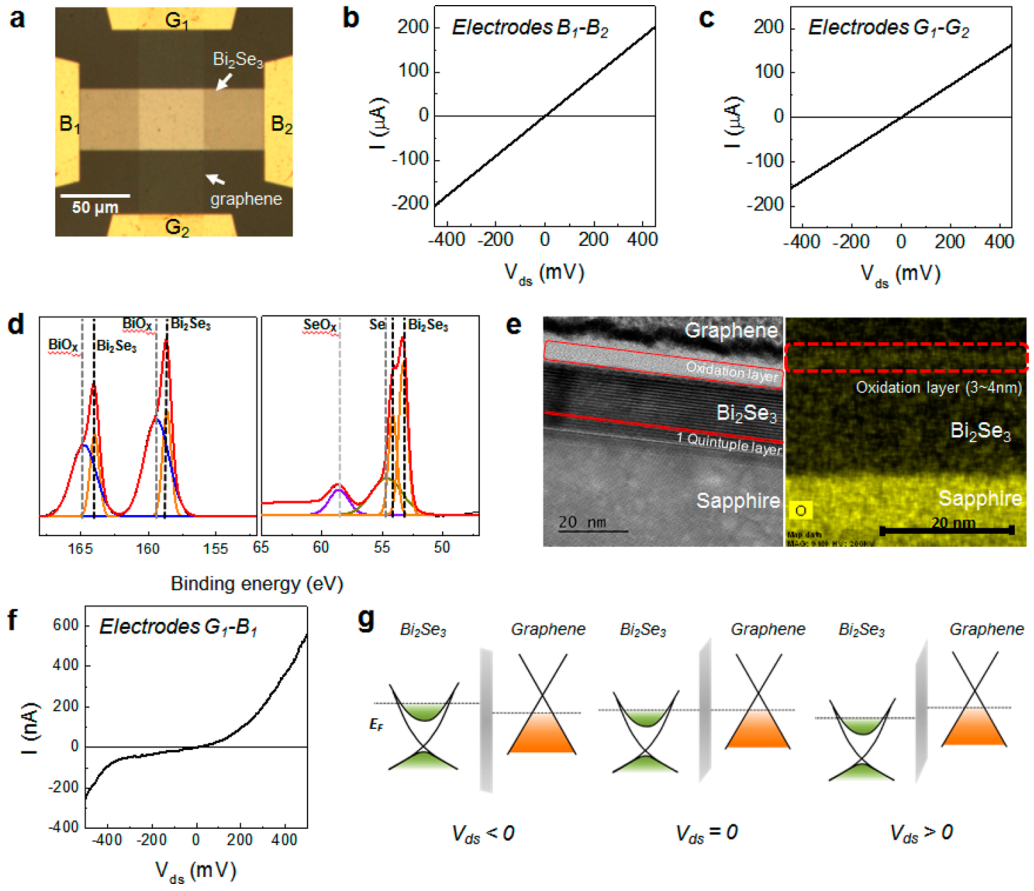

Figure 1. (a) Optical microscope image of the graphene−Bi_2Se_3 heterostructure photodetector based on an MBE-grown Bi_2Se_3 topological insulator and wet-transferred CVD graphene. (b, c) $I-V$ characteristics as a function of bias voltage applied across the two graphene contacts (b) and the two Bi_2Se_3 contacts (c). (d) XPS measurement spectra on Bi_2Se_3 with a BiO_x peak (left) and SeO_x peak (right) (e) Cross-sectional TEM image of Bi_2Se_3 (left) and oxygen element image (right). (f) $I-V$ characteristics as a function of bias voltage applied across the graphene−Bi_2Se_3 contacts showing a rectifying junction property at the interface between graphene and Bi_2Se_3. (g) Schematic band diagrams corresponding to panel f under forward and reverse bias. Black dashed lines indicate the Fermi levels of the graphene and Bi_2Se_3.

these structures is to experimentally achieve a photogating effect through efficient hot-carrier separation (see below for a more detailed discussion). For example, prior investigations showed that integrating a high-mobility graphene layer with a strongly light absorbing layer, e.g., colloidal quantum dots[12] and epitaxial growth of Bi_2Te_3[16] nanocrystals, demonstrated a record-high responsivity of 10^7 and 35 A W^{-1}, respectively. The spectral response, on the other hand, is primarily determined by the energy level spacing of quantum dots and Bi_2Te_3 nanocrystals, typically in a short-wavelength region of IR light. To detect mid-IR photons, these methods impose technical limitations on a detector's working area because of the long-wavelength nature of the mid-IR photons. In this work, we achieved mid-IR photodetection also covering near-IR regimes with a record-high responsivity at room temperature by integrating graphene and Bi_2Se_3 with small band gap (~300 meV)[17] for effective sensing of the mid-IR range. Unlike a recent mid-IR photodetector based on black phosphorus, which demonstrated a responsivity of 82 A W^{-1} at an extremely small incident power of 1 nW,[18] our device operates at a reasonable incident power regime of μW with no photocurrent saturation at such high incident power. Combined with the intrinsic tunnel barrier and a high-capacitance ion-gel gating to operate the graphene conducting channel at low voltage, the results show a promising route toward simple, efficient, and fast photodetection using low-dimensional heterostructures.

We first discuss the operation principle of our graphene−Bi_2Se_3 photodetector. Figure 1a is an optical microscopy image of the graphene−Bi_2Se_3 device used in this work. The device consists of 25 quintuple layers of a Bi_2Se_3 topological insulator grown by a molecular beam epitaxy (MBE) technique on a sapphire substrate and a wet-transferred[19] chemical vapor deposition (CVD)-grown top graphene layer (see Methods section for details on the device fabrication). Each quintuple layer of Bi_2Se_3 is a sequence of Se−Bi−Se−Bi−Se atomic layers.[20] In this device, the Bi_2Se_3 layer functions as a broadband IR light absorber supplying holes in the graphene, and the graphene functions as a high-mobility charge transport layer as well as a light absorption layer. All measurements are performed at room temperature in ambient conditions. The linear $I-V$ transfer curves in Figure 1b and c indicate ohmic (nonrectifying) characteristics between the electrodes connecting the Bi_2Se_3 and graphene (B_1-B_2 and G_1-G_2, respectively).

The photogating effect is based on the photoinduced adjustment of the carrier density Δn resulting in its conductance modulation $\Delta\sigma = e\Delta n\mu$,[21] where e is the elementary charge and μ is the mobility. In this simple relation, it is apparent that high-mobility graphene is a promising candidate for the conductance modulation channel. On the

DOI: 10.1021/acsphotonics.6b00972
ACS Photonics 2017, 4, 482−488

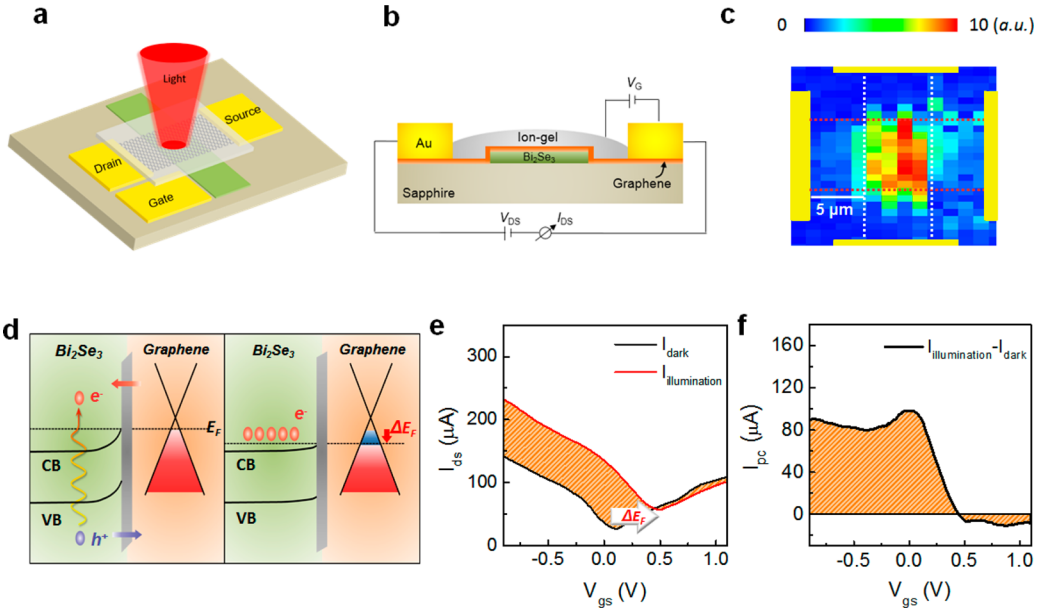

Figure 2. Photoresponse measurement of the graphene–Bi_2Se_3 heterostructure device. (a) Schematic device structure including the side gate, ionic gel, and the light illumination configuration. The laser wavelength is 3.5 μm with a spot diameter of 30 μm (fwhm), positioning the center of the cross-section of the graphene–Bi_2Se_3 layers. (b) Schematic transfer curve measurement circuit using the ion-gel gate bias voltage (V_{gs}) and the graphene bias voltage. The potential of the bottom Bi_2Se_3 layer was allowed to float, while the current of the top graphene transistor was measured with V_{ds} = 0.5 V. (c) Scanning photocurrent image of the graphene–Bi_2Se_3 with an excitation wavelength of 800 nm. Bi_2Se_3 and graphene layers are represented by red and white dotted lines, respectively. Yellow squares represent electrodes of each layer. The spot size of the 800 nm short pulse is 1 μm (fwhm). (d) Schematic band diagram and photoexcited hot-carrier transfer mechanism under light illumination. Electrons and holes are represented by red and blue dots, respectively. Vertical arrows represent photoexcitation, and lateral arrows represent tunneling of hot electron (red arrow) and hole (blue arrow). (e) I–V_{gs} characteristics of the measured graphene photodetector with (red, $I_{illumination}$) and without (black, I_{dark}) 50 μW mid-IR light illumination. (f) Gate-dependent photocurrent $I_{pc} = I_{illumination} - I_{dark}$ at 50 μW mid-IR laser power.

other hand, Δn is typically achieved by hot-carrier separation with an energy barrier (Schottky or tunneling) at the interface. Provided that the electron and hole tunneling rate is different due to the asymmetric interface barrier, the charges trapped in the Bi_2Se_3 layer of the heterostructure provide an electrostatic potential to the graphene layer, leading to Δn in graphene, i.e., a photogating effect.[22] Therefore, the crucial element enabling the photogating effect is the junction characteristics between graphene and Bi_2Se_3. Because of the surface reactivity, it is well known that surface oxidation typically occurs in air-exposed Bi_2Se_3; that is, a tunneling barrier is naturally formed.[23−25] Indeed, we performed X-ray photoelectron spectroscopy (XPS) and transmission electron microscopy (TEM) measurement (Figure 1d and e) to confirm the existence of an oxidation layer at the surface of the Bi_2Se_3. Peaks of bismuth oxide (BiO_x) and selenium oxide (SeO_x) are clearly shown, and most of them are located on the Bi_2Se_3 surface as an oxidized layer. The built-in potential is generated due to the work function difference between the two materials (4.6 and 4.0 eV at ambient conditions[23−25] for graphene and Bi_2Se_3, respectively). Actually, this oxidized barrier causes degradation of the surface topological state. Prior studies[17,26] have maintained an ultrahigh vacuum ($\sim 10^{-9}$ mbar) for the sample growth or removed it with surface plasma treatments to make ohmic contacts on Bi_2Se_3. In contrast, we have used this barrier to realize a simple rectifying tunneling junction between graphene and Bi_2Se_3. Although spin–orbit coupling induced operating and band hybridization in graphene–topological insulator van der Waals heterostructures was theoretically predicted in recent studies,[27,28] we believe that this effect is negligible in our structure in that it is strictly the case when the interface is ideally clean (no oxide layer) and crystal orientation is matched between the two materials, of which experimental realization seems to be extremely difficult to achieve. The naturally formed tunneling barrier at the interface also prevents proximity of the two materials to have a strong interaction. The nonlinear I–V curve between Bi_2Se_3 and graphene shown in Figure 1d clearly indicates a rectifying junction supporting a tunneling current, of which the schematic of the junction band diagram is illustrated in Figure 1e. Note that the tunneling current in Figure 1d is asymmetric under forward and reverse bias, which is indispensable for realizing a photogating effect.

To verify the proposed operating principle, we measure the photoresponse of the graphene/Bi_2Se_3 heterostructure (Figure 2a) using an ion-gel (see Methods for details on the ion-gel information) side gate (Figure 2b).[29−31] Current–voltage output characteristics (I–V measurements) were measured by using a Keithley 2400 and a Keithley 2450 sourcemeter, which were used to apply a source–drain voltage and a gate–source voltage, respectively. Figure 2c is a scanning two-dimensional (2D) photocurrent image measured with a 50 fs, 800 nm pulse (Coherent RegA 9050); the diffraction-limited spot size is estimated to be 1 μm (fwhm). The data show that the photocurrent is generated dominantly in the overlapped region of the graphene–Bi_2Se_3 junction, which ensures that the major photocurrent is generated at this junction. After checking the photoactive overlap junction, we have turned our attention to the mid-IR photoresponse. For the mid-IR measurement, a wavelength-tunable mid-IR pulse (pulse width of ~320 fs) was generated via a difference-frequency generator (Coherent DFG 9850) and an optical parametric amplifier (Coherent OPA 9850), in which a 250 kHz regenerative amplifier (Coherent

DOI: 10.1021/acsphotonics.6b00972
ACS Photonics 2017, 4, 482−488

RegA 9050) was used as a "seed" laser. The power was measured by a PbSe detector (Thorlabs PDA20H) and calibrated by a thermopile broadband power meter (Thorlab PM100D). More detailed characterization of the ultrashort mid-IR pulse was presented in our previous mid-IR spectroscopy report.[32]

First, we focus on the mid-IR photoresponse; note that all of the transport and photoresponse data are obtained from the device shown in Figure 1a, other than the 2D photocurrent image shown in Figure 2c. The photogating effect was measured on two electrodes of graphene by sweeping the ion-gel gate bias (V_{gs}) with and without mid-IR light illumination, λ = 3.5 μm. Here, the focusing optics were a calcium fluoride D-coating lens and a barium fluoride antireflection coating lens with a spot size of 30 μm. The photoexcitation occurs in both graphene and Bi_2Se_3, and hot carriers are separated efficiently into graphene and Bi_2Se_3 via tunneling. Holes easily tunnel from Bi_2Se_3 to graphene due to the asymmetric potential (Figure 2d, left panel). Consequently, negative charges are accumulated in the bottom Bi_2Se_3 (Figure 2d, right panel), resulting in Δn on the top graphene transistor. In particular, the graphene channel has a high carrier mobility (up to 4000 $cm^2\ V^{-1}\ s^{-1}$ in CVD-grown graphene),[19,33] so that its conductance is very sensitive to the modulated carrier density. As shown in Figure 2e, the transfer curve under light illumination ($I_{illumination}$) with a laser power P of 50 μW shifts dramatically toward positive V_{gs} compared to the dark transfer curve I_{dark}, and a horizontal shift of the Dirac point (ΔV_{shift}) of 0.68 V is observed. This is direct evidence of a strong photogating effect; that is, the electrons trapped in the Bi_2Se_3 layer lead to the increased hole density in graphene because the trapped electrons act like a gate bias. Thus, we plot the gate-tunable photocurrent $I_{pc} = I_{illumination} - I_{dark}$ (Figure 2f) as a function of V_{gs}, showing a clear zero-crossing of I_{pc} due to the horizontal shift of the Dirac point.

Figure 3a shows the I_{pc} as a function of the mid-IR light power at two representative gate biases. The slope $dI_{pc}/dP_{mid\text{-}IR}$ shows a responsivity of 1.97 A W^{-1} at V_{gs} = 0.02 V. It is a record-high value compared with other photodetectors at the same incident power and shows steady responsivity over a broad incident power region. It is obvious that lower incident power is advantageous for obtaining higher responsivity since the photoexcited carrier, which makes an opposite electric field to the built-in field at the graphene–Bi_2Se_3 junction, increases at higher incident power. We note that recent photodetectors show high responsivity at very low incident power, but the responsivity flatness could not be maintained at higher incident power, showing limited performance as far as a practical photodetector.[16,18] More quantitatively, we examine Δn estimated by ΔV_{shift} upon light illumination. The graphene Fermi-level shift (ΔE_f) can be calculated using the dispersion relation[34,35]

$$\Delta E_F = \hbar v_F \sqrt{\pi C \frac{\Delta V_{shift}}{e}} \quad (1)$$

where $\hbar$ is the Planck constant, v_F is the graphene Fermi velocity, $C \approx 5.17\ \mu F\ cm^{-2}$ is the ion-gel gate capacitance,[31] and e is the electron charge. Figure 3b shows ΔE_f (upper panel) and a corresponding $\Delta n = C\Delta V_{shift}/e$ (bottom panel) as a function of the mid-IR laser power. Solid and dashed lines in the panels show the expected ΔE_f and Δn variation as a function of light power for the case of perfect *internal* quantum

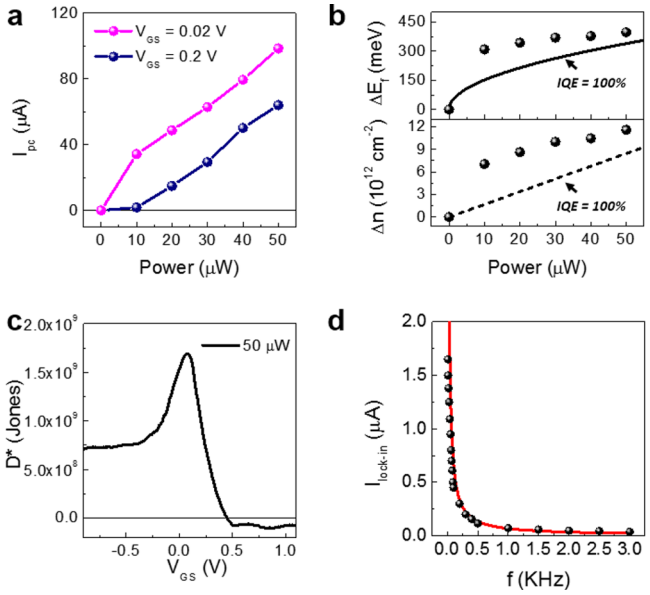

Figure 3. (a) I_{pc} as a function of laser power at V_{gs} = 0.02 V (purple dots) and 0.2 V (blue dots) with 3.5 μm photon wavelength. (b) The Fermi-level shift, ΔE_f (top panel), and the corresponding photo-induced carrier density, Δn (bottom panel), of graphene as a function of light power. They are extracted by shifts of charge neutral voltage, ΔV_{shift}. The solid (dashed) curve of the top (bottom) panel shows the expected ΔE_f (Δn) for graphene without Bi_2Se_3 assuming perfect internal quantum efficiency (IQE). (c) Specific detectivity D^* as a function of V_{gs} (see main text for more discussion). (d) Lock-in detected photocurrent signal ($I_{lock\text{-}in}$) as a function of chopping frequency f for measurement of photoresponse time (τ_r). The measurement is performed using a mechanically chopped laser with λ = 3.5 μm, laser power P = 50 μW, and V_{ds} = 0.3 V. The red solid curve shows a fit to eq S1 with the best fit parameter τ_r = 4 μs.

efficiency (IQE), where one takes only the graphene's intrinsic optical absorption of $2Z_0\sigma_0/(n_s + 1) \approx 1.8\%$[36] into account and assumes perfect e–h pair generation/detection without recombination, where Z_0 is the vacuum impedance, $\sigma_0 = \pi e^2/2h$ is the quantum conductivity, and n_S = 1.67 is the refractive index of the sapphire substrate at a wavelength of 3.5 μm.[37] The measured values for ΔE_f and Δn greatly exceeding an ideal IQE scenario, especially more than a factor of 3 at a low power limit, strongly indicate that an electronic gain exists due to extra charges supplied (or photogated) from the Bi_2Se_3 layer.

To further demonstrate the device performance, we convert the responsivity to the specific detectivity, $D^* = R \times A^{1/2}/(2eI_{dark})^{1/2}$ [cm·$Hz^{1/2}$ W^{-1} or Jones], reflecting the signal-to-noise ratio of the device, where R is the responsivity and A is the illuminated area of the device. Figure 3c shows D^* as a function of the gate bias voltage. The maximum value of D^* is 1.7×10^9 cm·$Hz^{1/2}$/W for V_{gs} = 0.08 V at room temperature. Although this value is comparable to that of commercial IR photodetectors based on low-band-gap semiconductor compounds,[38] it is considerably high because our detector operates in the mid-IR region at room temperature. We also examined the dynamics of the photoresponse (Supporting Information Figure S3), in which we assume a square light pulse of duty cycle 50% with frequency f is generated by a mechanical chopper (upper diagram), while the time dependence of the photocurrent from the device is low-pass-filtered due to a finite response time, τ_r, whose rms

DOI: 10.1021/acsphotonics.6b00972
ACS Photonics 2017, 4, 482–488

value is measured via a lock-in amplifier (SR850). Thus, we model the rms current detected in lock-in as

$$I_{\text{lock-in}}(f) = \sqrt{\frac{1}{f}\int_0^{1/f}\left[I_{\text{sat}}\left\{(1-e^{-t/\tau_r})\theta\left(\frac{1}{2f}-t\right)+(1-e^{-1/2f\cdot\tau_r})e^{-(t-\frac{1}{2f})/\tau_r}\theta\left(t-\frac{1}{2f}\right)\right\}\right]^2 dt} \quad (2)$$

where $\theta(t)$ is the Heaviside step function, and the above equation is used fit to the measured $I_{\text{lock-in}}(f)$ to extract $\tau_r = 4\ \mu$s for our device. The response time (τ_r) of the device, which is another figure of merit, is shown in Figure 3d. The data were taken by measuring I_{pc} with a chopped laser beam ($\lambda = 3.5\ \mu$m, $P = 50\ \mu$W) with a variable chopping frequency. Assuming a single-time characteristic response of the device, we model the measured signal by the time-averaged rms value of a low-pass-filtered current signal. By fitting the model curve to the measured values, we estimated the quantum efficiency η and the photoconductive gain G_p in the following way. The relationship between photoinduced carrier density Δn and η follows the equation $\Delta n = \tau_r \eta \Phi_p$, where $\tau_r = 4\ \mu$s is the device response time estimated above and Φ_p is the incident light photon flux. We estimate $\eta = 2.3\%$ of our device at a 50 μW mid-IR light power. G_p is the number of detected charge carriers per single incident photon and is calculated by $G_p = (I_{pc}/e)/(\eta\Phi_p)$. We obtained a G_p of 30, and this indicates direct evidence of the additional gain mechanism arising from a photogating effect. Table 1 summarizes the key parameters of our device compared with various graphene-based mid-IR photodetectors.[11,39−41] The high responsivity, low working bias voltage, fast response time, and simple fabrication with an intrinsic tunneling barrier make our graphene−Bi_2Se_3 heterostructure a promising platform to develop highly efficient mid-IR photodetectors.

Table 1. Performance Parameters in Various Graphene-Based Mid-IR Photodetectors

device structure	responsivity (R) (A W^{-1})	operating V at max. R	λ (μm)	ref
graphene/Bi_2Se_3 heterojunction	1.97	V_{gs} = 0.02 V, V_{ds} = 0.5 V	3.5	this work
graphene quantum-dot-like-array structure at 12 K	0.4	V_{ds} = 0.02 V	10	12
graphene coupled to Si waveguide	0.13	V_{ds} = 1.5 V	2.75	40
graphene/metallic antenna heterojunction	0.4	V_{gs} = 5 V, V_{ds} = 0.6 V	4.45	11
graphene double-layer heterostructure	1.1	V_{gs} = −60 V, V_{ds} = 1.5 V	3.2	41

We now turn to discuss the IR spectral range of our photodetector by measuring wavelength-dependent responsivity. Figure 4a and b show I_{pc} as a function of laser power at two gate biases for 2.07 μm (Figure 4a) and 1.3 μm (Figure 4b) photon wavelengths covering both the near-IR and IR range. Here, the near-IR pulses centered at 1.30 and 2.07 μm were directly generated in an optical parametric amplifier (Coherent OPA 9850). An even larger responsivity of about a factor of 4 times (1.5 times) enhancement at 1.30 μm (2.07 μm) compared to the 3.5 μm wavelength suggests that the device responsivity is closely related to hot-carrier injection and tunneling rate, which is proportional to the photoexcited carrier energy. Significantly, the near-IR responsivity of the device reaches 2.7 A W^{-1} at $\lambda = 2.07\ \mu$m (Figure 4a) and 8.18 A W^{-1} at $\lambda = 1.3\ \mu$m (Figure 4b) at room temperature. The strong photogating effect and gate modulation of the photoresponse indicated by large enhancements of ΔE_f and Δn (Figure 4c and d) compared with graphene without Bi_2Se_3 are again clearly observed in the near-IR regime (see Supporting Information Figures S5 and S6 for the complete gate-tunable photocurrent response for 2.07 and 1.3 μm).

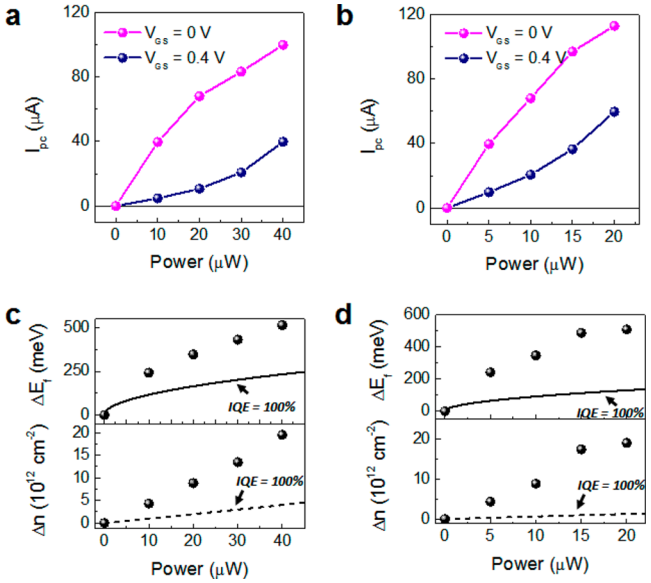

Figure 4. Photoresponse of the heterostructure graphene−Bi_2Se_3 photodetector with near-IR light illumination. (a, b) Photocurrent as a function of laser power at V_{gs} = 0 (purple) and 0.2 V (blue) with illumination of light having a 2.07 μm (a) and 1.30 μm (b) photon wavelength. (c, d) ΔE_f (upper panel) and the corresponding Δn (bottom panel) of graphene as a function of light power with illumination of light having a 2.07 μm (a) and 1.30 μm (b) photon wavelength. The solid (dashed) curve in the top (bottom) panel in (c) and (d) shows the expected ΔE_f (Δn) for graphene without Bi_2Se_3 assuming perfect internal quantum efficiency (IQE).

Finally, it is worth discussing the difference between the photocurrent response using a short pulse and the continuous wave (cw) laser excitation. For the mid-IR and IR photoresponse measurements, we have used wavelength-tunable femtosecond laser pulses. In general, a short-pulse laser has an intense energy per pulse, which can instantaneously heat the graphene−Bi_2Se_3 heterostructures and effectively generate more thermoelectric current than the cw laser source. Indeed, prior studies have investigated the thermoelectric characteristics of graphene[7] and revealed more thermoelectric current is generated compared to the short-pulse excitation. When no source−drain bias is applied, the primary photoresponse of graphene follows the photothermoelectric effect[7,42] due to the small heat capacity of carbon atoms. However, the main mechanism of our device is the photovoltaic effect under

DOI: 10.1021/acsphotonics.6b00972
ACS Photonics 2017, 4, 482−488

applied source−drain bias, and it is proportional to the generated electron−hole pairs depending on both the incident photon energy and the average power of excitation pulses.[41,43,44] Also, the short-pulse laser is focused on the cross-section of graphene−Bi_2Se_3, which is in the middle of the channel to minimize the possible thermoelectric effect. Therefore, a quantitatively negligible difference of the photocurrent is expected in using the pulse laser compared to the cw laser.

In summary, broadband light absorption of small-band-gap Bi_2Se_3 combined with an intrinsically formed tunnel barrier and high mobility graphene enables sensitive photodetection covering the mid-IR and near-IR regimes at room temperature. A strong photogating effect and efficient carrier separation show a record-high responsivity at mid-IR wavelength. In fact, Bi_2Se_3 is an exemplary three-dimensional topological insulator, where a spin-momentum-locked metallic surface state coexists with low-band-gap insulating bulk states[45,46] due to band inversion induced by a strong spin−orbit coupling. Indeed, light excitation can strongly interact with the surface electrons of Bi_2Se_3, and helicity-dependent spin photocurrent control including spin injection and detection is of current interest.[47] Although we use an unpolarized light source, we do not rule out the possibility of photoinduced surface electron and hole separation at the Bi_2Se_3/graphene interface. We expect that the device platform developed here with a natural tunnel barrier can also be used for efficient spin injection and detection.[48] In this respect, it might be possible to conduct a new spin-optoelectronics experiment by inducing a spin-polarized helicity-dependent photocurrent in topological insulators using circularly polarized light and detecting nonlocal spin voltage, for example, with ferromagnetic electrodes prepared on the graphene layer. Even with photoinduced charge transport only, our results provide a novel route to realize graphene-based high-performance mid-IR photodetectors at room temperature.

METHODS

Device Fabrication. The graphene and the Bi_2Se_3 used in this work were synthesized by the CVD method and MBE technique, respectively. The sample qualities are characterized by XPS measurement and TEM measurement. They show the existence of an oxide layer between Bi_2Se_3 and graphene. The bottom Bi_2Se_3 was synthesized on a sapphire substrate, and the top graphene was transferred onto the Bi_2Se_3 by a wet transfer method. A rectangular pattern for both graphene and Bi_2Se_3 was formed by standard photolithography and reactive ion etching. Cr/Au (5/50 nm) electrodes on graphene and the Bi_2Se_3 were metalized by a commercial thermal evaporator.

Ion-Gel Information. The ion-gel that we used in our device consists of a room-temperature ionic liquid ([EMIN][TFSI]) and gelating triblock copolymer ([PS-PMMA-PS]), which exhibits an extremely high capacitance of 5.17 μF cm^{-2}. The ionic liquid, triblock copolymer, and ethyl acetate solvent are mixed according to a mass ratio of 9.3:0.7:90, respectively. Then, to make a uniform mixture, it was put on a spin coater at 1200 rpm for 2 h.

ASSOCIATED CONTENT

Supporting Information

The Supporting Information is available free of charge on the ACS Publications website at DOI: 10.1021/acsphotonics.6b00972.

Rectangular function generation by mechanical chopping and the corresponding output photocurrent signal response; $I-V_{GS}$ characteristics $I_{illumination}$ and I_{pc} at various light power with 3.5, 2.07, and 1.3 μm light wavelengths (PDF)

AUTHOR INFORMATION

Corresponding Authors

*E-mail: dohunkim@snu.ac.kr.
*E-mail: hychoi@yonsei.ac.kr.

ORCID

Moon-Ho Jo: 0000-0002-3160-358X
Hyunyong Choi: 0000-0003-3295-1049

Author Contributions

▽J. Kim and S. Park contributed equally to this work.

Notes

The authors declare no competing financial interest.

ACKNOWLEDGMENTS

J.K., S.P., S.S., S.C., C.I., J.P., J.L., M.N., and H.C. were supported by the National Research Foundation of Korea (NRF) through the government of Korea (MSIP) (Grant Nos. NRF-2015R1A2A1A10052520, NRF-2016R1A4A1012929), and Global Frontier Program (2014M3A6B3063709). J.S. and M.J. were supported by Institute for Basic Science (IBS), Korea, under the Project Code IBS-R014-G1-2016-a00. D.K. was supported by the Basic Science Research Program through the NRF funded by the Ministry of Science, ICT & Future Planning (Grant No. NRF-2015R1C1A1A02037430). S.C. and M.H. were supported by the Nation Research Foundation of Korea (NRF) through the government of Korea (MSIP) (Grant No. NRF-2016R1A4A1012929). N.K., M.S., J.M., and S.O. are supported by the National Science Foundation of the USA (DMR-1308142 and EFMA-1542798) and the Gordon and Betty Moore Foundation's EPiQS Initiative (GBMF4418).

REFERENCES

(1) Rogalski, A. Infrared Detectors: Status and Trends. *Prog. Quantum Electron.* **2003**, *27*, 59−210.
(2) Soref, R. Mid-Infrared Photonics in Silicon and Germanium. *Nat. Photonics* **2010**, *4*, 495−497.
(3) Clark, J.; Lanzani, G. Organic Photonics for Communications. *Nat. Photonics* **2010**, *4*, 438−446.
(4) Capasso, F.; Paiella, R.; Martini, R.; Colombelli, R.; Gmachl, C.; Myers, T. L.; Taubman, M. S.; Williams, R. M.; Bethea, C. G.; Unterrainer, K.; Hwang, H. Y.; Sivco, D. L.; Cho, A. Y.; Sergent, A. M.; Liu, H. C.; Whittaker, E. A. Quantum Cascade Lasers: Ultrahigh-Speed Operation, Optical Wireless Communication, Narrow Linewidth, and Far-Infrared Emission. *IEEE J. Quantum Electron.* **2002**, *38*, 511−532.
(5) Zecchina, A.; Arean, C. Islands, B. Diatomic Molecular Probes for Mid-IR Studies of Zeolites. *Chem. Soc. Rev.* **1996**, *25*, 187−197.
(6) Sun, D.; Wu, Z.-K.; Divin, C.; Li, X.; Berger, C.; de Heer, W. A.; First, P. N.; Norris, T. B. Ultrafast Relaxation of Excited Dirac Fermions in Epitaxial Graphene Using Optical Differential Transmission Spectroscopy. *Phys. Rev. Lett.* **2008**, *101*, 157402.
(7) Graham, M. W.; Shi, S.-F.; Ralph, D. C.; Park, J.; McEuen, P. L. Photocurrent Measurements of Supercollision Cooling in Graphene. *Nat. Phys.* **2013**, *9*, 103−108.
(8) Liu, Y.; Cheng, R.; Liao, L.; Zhou, H.; Bai, J.; Liu, G.; Liu, L.; Huang, Y.; Duan, X. Plasmon Resonance Enhanced Multicolour Photodetection by Graphene. *Nat. Commun.* **2011**, *2*, 579.
(9) Low, T.; Avouris, P. Graphene Plasmonics for Terahertz to Mid-Infrared Applications. *ACS Nano* **2014**, *8*, 1086−1101.

DOI: 10.1021/acsphotonics.6b00972
ACS Photonics 2017, 4, 482−488

(10) Low, T.; Guinea, F.; Yan, H.; Xia, F.; Avouris, P. Novel Midinfrared Plasmonic Properties of Bilayer Graphene. *Phys. Rev. Lett.* **2014**, *112*, 116801.
(11) Yao, Y.; Shankar, R.; Rauter, P.; Song, Y.; Kong, J.; Loncar, M.; Capasso, F. High-Responsivity Mid-Infrared Graphene Detectors with Antenna-Enhanced Photocarrier Generation and Collection. *Nano Lett.* **2014**, *14*, 3749−3754.
(12) Konstantatos, G.; Badioli, M.; Gaudreau, L.; Osmond, J.; Bernechea, M.; de Arquer, F. P. G.; Gatti, F.; Koppens, F. H. L. Hybrid Graphene-Quantum Dot Phototransistors with Ultrahigh Gain. *Nat. Nanotechnol.* **2012**, *7*, 363−368.
(13) Gabor, N.; Song, J.; Ma, Q.; Nair, N. Hot Carrier-Assisted Intrinsic Photoresponse in Graphene. *Science* **2011**, *334*, 648−652.
(14) Park, J.; Ahn, Y. H.; Ruiz-Vargas, C. Imaging of Photocurrent Generation and Collection in Single-Layer Graphene. *Nano Lett.* **2009**, *9*, 1742−1746.
(15) Song, J. C. W.; Rudner, M. S.; Marcus, C. M.; Levitov, L. S. Hot Carrier Transport and Photocurrent Response in Graphene. *Nano Lett.* **2011**, *11*, 4688−4692.
(16) Qiao, H.; Yuan, J.; Xu, Z.; Chen, C.; Lin, S.; Wang, Y.; Song, J.; Liu, Y.; Khan, Q.; Hoh, H. Y.; Pan, C. X.; Li, S.; Bao, Q. Broadband Photodetectors Based on Graphene-Bi2Te3 Heterostructure. *ACS Nano* **2015**, *9*, 1886−1894.
(17) Cao, Y.; Waugh, J. a.; Zhang, X.-W.; Luo, J.-W.; Wang, Q.; Reber, T. J.; Mo, S. K.; Xu, Z.; Yang, A.; Schneeloch, J.; Gu, G. D.; Brahlek, M.; Bansal, N.; Oh, S.; Zunger, A.; Dessau, D. S. Mapping the Orbital Wavefunction of the Surface States in Three-Dimensional Topological Insulators. *Nat. Phys.* **2013**, *9*, 499−504.
(18) Guo, Q.; Pospischil, A.; Bhuiyan, M.; Jiang, H.; Tian, H.; Farmer, D.; Deng, B.; Li, C.; Han, S. J.; Wang, H.; Xia, Q.; Ma, T. P.; Mueller, T.; Xia, F. Black Phosphorus Mid-Infrared Photodetectors with High Gain. *Nano Lett.* **2016**, *16*, 4648−4655.
(19) Kim, K. S.; Zhao, Y.; Jang, H.; Lee, S. Y.; Kim, J. M.; Ahn, J.-H.; Kim, P.; Choi, J.-Y.; Hong, B. H. Large-Scale Pattern Growth of Graphene Films for Stretchable Transparent Electrodes. *Nature* **2009**, *457*, 706−710.
(20) Zhang, H.; Liu, C.-X.; Qi, X.-L.; Dai, X.; Fang, Z.; Zhang, S.-C. Topological Insulators in Bi2Se3, Bi2Te3 and Sb2Te3 with a Single Dirac Cone on the Surface. *Nat. Phys.* **2009**, *5*, 438−442.
(21) Koppens, F. H.; Mueller, T.; Avouris, P.; Ferrari, a C.; Vitiello, M. S.; Polini, M. Photodetectors Based on Graphene, Other Two-Dimensional Materials and Hybrid Systems. *Nat. Nanotechnol.* **2014**, *9*, 780−793.
(22) Buscema, M.; Island, J. O.; Groenendijk, D. J.; Blanter, S. I.; Steele, G. A.; van der Zant, H. S.; Castellanos-Gomez, A. Photocurrent Generation with Two-Dimensional van Der Waals Semiconductors. *Chem. Soc. Rev.* **2015**, *44*, 3691−3718.
(23) Edmonds, M. T.; Hellerstedt, J. T.; Tadich, A.; Schenk, A.; Donnell, K. M. O.; Tosado, J.; Butch, N. P.; Syers, P.; Paglione, J.; Fuhrer, M. S. Stability and Surface Reconstruction of Topological Insulator Bi2Se3 on Exposure to Atmosphere. *J. Phys. Chem. C* **2014**, *118*, 20413−20419.
(24) Kong, D.; Cha, J. J.; Lai, K.; Peng, H.; Analytis, J. G.; Meister, S.; Chen, Y.; Zhang, H.-J.; Fisher, I. R.; Shen, Z.-X.; Cui, Y. Rapid Surface Oxidation as a Source of Surface Degradation Factor for Bi_2Se_3. *ACS Nano* **2011**, *5*, 4698−4703.
(25) Zhang, L.; Yan, Y.; Wu, H.; Liao, Z.; Yu, D. Gate-Tunable Tunneling Resistance in Graphene/Topological Insulator Vertical Junctions. *ACS Nano* **2016**, *10*, 3816−3822.
(26) Di Pietro, P.; Ortolani, M.; Limaj, O.; Di Gaspare, A.; Giliberti, V.; Giorgianni, F.; Brahlek, M.; Bansal, N.; Koirala, N.; Oh, S.; Calvani, P.; Lupi, S. Observation of Dirac Plasmons in a Topological Insulator. *Nat. Nanotechnol.* **2013**, *8*, 556−560.
(27) Kou, L.; Yan, B.; Hu, F.; Wu, S. C.; Wehling, T. O.; Felser, C.; Chen, C.; Frauenheim, T. Graphene-Based Topological Insulator with an Intrinsic Bulk Band Gap above Room Temperature. *Nano Lett.* **2013**, *13*, 6251−6255.
(28) Rajput, S.; Li, Y.-Y.; Weinert, M.; Li, L. Indirect Interlayer Bonding in Graphene−Topological Insulator van Der Waals Heterostructure: Giant Spin−Orbit Splitting of the Graphene Dirac States. *ACS Nano* **2016**, *10*, 8450−8456.
(29) Cho, J. H.; Lee, J.; Xia, Y.; Kim, B.; He, Y.; Renn, M. J.; Lodge, T. P.; Daniel Frisbie, C. Printable Ion-Gel Gate Dielectrics for Low-Voltage Polymer Thin-Film Transistors on Plastic. *Nat. Mater.* **2008**, *7*, 900−906.
(30) Kim, B. J.; Jang, H.; Lee, S.-K.; Hong, B. H.; Ahn, J.-H.; Cho, J. H. High-Performance Flexible Graphene Field Effect Transistors with Ion Gel Gate Dielectrics. *Nano Lett.* **2010**, *10*, 3464−3466.
(31) Lee, S.-K.; Kabir, S. M. H.; Sharma, B. K.; Kim, B. J.; Cho, J. H.; Ahn, J.-H. Photo-Patternable Ion Gel-Gated Graphene Transistors and Inverters on Plastic. *Nanotechnology* **2014**, *25*, 14002.
(32) Cha, S.; Sung, J. H.; Sim, S.; Park, J.; Heo, H.; Jo, M.-H.; Choi, H. 1s-Intraexcitonic Dynamics in Monolayer MoS2 Probed by Ultrafast Mid-Infrared Spectroscopy. *Nat. Commun.* **2016**, *7*, 10768.
(33) Geim, A. K. Graphene: Status and Prospects. *Science* **2009**, *324*, 1530−1534.
(34) Lee, E. J. H.; Balasubramanian, K.; Weitz, R. T.; Burghard, M.; Kern, K. Contact and Edge Effects in Graphene Devices. *Nat. Nanotechnol.* **2008**, *3*, 486−490.
(35) Xu, X.; Gabor, N. M.; Alden, J. S.; Van Der Zande, A. M.; McEuen, P. L. Photo-Thermoelectric Effect at a Graphene Interface Junction. *Nano Lett.* **2010**, *10*, 562−566.
(36) Kim, J.; Oh, J.; In, C.; Lee, Y. S.; Norris, T. B.; Jun, S. C.; Choi, H. Unconventional Terahertz Carrier Relaxation in Graphene Oxide: Observation of Enhanced Auger Recombination due to Defect Saturation. *ACS Nano* **2014**, *8*, 2486−2494.
(37) Malitson, I. H. Refraction and Dispersion of Synthetic Sapphire. *J. Opt. Soc. Am.* **1962**, *52*, 1377−1379.
(38) Rogalski, A., Piotrowski, J. *High-Operating-Temperature Infrared Photodetectors*; SPIE Press: Bellingham, WA, 2007;.
(39) Zhang, B. Y.; Liu, T.; Meng, B.; Li, X.; Liang, G.; Hu, X.; Wang, Q. J. Broadband High Photoresponse from Pure Monolayer Graphene Photodetector. *Nat. Commun.* **2013**, *4*, 1811.
(40) Wang, X.; Cheng, Z.; Xu, K.; Tsang, H. K.; Xu, J.-B. High-Responsivity Graphene/silicon-Heterostructure Waveguide Photodetectors. *Nat. Photonics* **2013**, *7*, 888−891.
(41) Liu, C.-H.; Chang, Y.-C.; Norris, T. B.; Zhong, Z. Graphene Photodetectors with Ultra-Broadband and High Responsivity at Room Temperature. *Nat. Nanotechnol.* **2014**, *9*, 273−278.
(42) Betz, A. C.; Jhang, S. H.; Pallecchi, E.; Ferreira, R.; Fève, G.; Berroir, J.-M.; Plaçais, B. Supercollision Cooling in Undoped Graphene. *Nat. Phys.* **2013**, *9*, 109−112.
(43) Mueller, T.; Xia, F.; Avouris, P. Graphene Photodetectors for High-Speed Optical Communications. *Nat. Photonics* **2010**, *4*, 297−301.
(44) Gan, X.; Shiue, R.-J.; Gao, Y.; Meric, I.; Heinz, T. F.; Shepard, K.; Hone, J.; Assefa, S.; Englund, D. Chip-Integrated Ultrafast Graphene Photodetector with High Responsivity. *Nat. Photonics* **2013**, *7*, 883−887.
(45) Di Pietro, P.; Ortolani, M.; Limaj, O.; Di Gaspare, A.; Giliberti, V.; Giorgianni, F.; Brahlek, M.; Bansal, N.; Koirala, N.; Oh, S.; Calvani, P.; Lupi, S. Observation of Dirac Plasmons in a Topological Insulator. *Nat. Nanotechnol.* **2013**, *8*, 556−560.
(46) Okada, Y.; Madhavan, V. Topological Insulators: Plasmons at the Surface. *Nat. Nanotechnol.* **2013**, *8*, 541−542.
(47) McIver, J. W.; Hsieh, D.; Steinberg, H.; Jarillo-Herrero, P.; Gedik, N. Control over Topological Insulator Photocurrents with Light Polarization. *Nat. Nanotechnol.* **2011**, *7*, 96−100.
(48) Rashba, E. I. Theory of Electrical Spin Injection: Tunnel Contacts as a Solution of the Conductivity Mismatch Problem. *Phys. Rev. B: Condens. Matter Mater. Phys.* **2000**, *62*, R16267.

DOI: 10.1021/acsphotonics.6b00972
ACS Photonics 2017, 4, 482−488